Materials Today Chemistry 25 (2022) 100967

Contents lists available at ScienceDirect

Materials Today Chemistry

journal homepage: www.journals.elsevier.com/materials-today-chemistry/

Graphene fluoride as a conductive agent for Li-argyrodite electrolyte containing all-solid-state batteries

X. Dai [a], J.H. Song [b], J.E. Wang [a], X. Chen [c, **], D.K. Kim [b, *], D.J. Kim [a, ***]

[a] School of Chemistry, The University of New South Wales, Sydney 2052, Australia
[b] Department of Materials Science and Engineering, Korea Advanced Institute of Science and Technology (KAIST), Daejeon, 34141, Republic of Korea
[c] School of Environmental and Life Sciences, The University of Newcastle, Callaghan, NSW 2308, Australia

ARTICLE INFO

Article history:
Received 1 March 2022
Received in revised form
22 April 2022
Accepted 25 April 2022
Available online xxx

Keywords:
Solid-state electrolyte
Conductive agents
Interfacial stability
Microwave-induced exfoliation
Lithium fluoride

ABSTRACT

A sulfide-based Li-argyrodite, Li_6PS_5X (X = Cl, Br, I), is a promising solid-state electrolyte candidate for next-generation all-solid-state batteries. The compound features high ionic conductivity, which is attributed to the high polarizability of sulfur and anion site disorder, providing advantageous crystallographic geometries for Li-ions to occupy and diffuse. However, the chemical instability of Li_6PS_5Cl during cycling limits its implementation in practical applications. This study employs graphene fluoride as a conductive agent for the cathode composite to alleviate the undesirable decomposition reactions at the electrolyte interface. The combined measurements of time-dependent X-ray photoelectron spectroscopy and electrochemical analysis confirmed that graphene fluoride significantly enhances the chemical stability of the electrolyte interface, yielding a stable cycling performance.

1. Introduction

The application of lithium-ion batteries (LIBs) has widely expanded over the past two decades, from small electronic devices to electric vehicles. Compared to other rechargeable battery configurations, LIBs offer a large capacity, higher voltage, and longer cycle life. In addition, the recent development of new materials and engineering optimization has significantly increased the energy and power densities of LIBs. However, the safety perspective of LIBs has not been fully addressed yet. In fact, many safety issues are related to the flammable carbonate-based organic electrolyte that overheating during the charge and discharge process triggers thermal runaway. This safety risk becomes more critical as the cell size increases and more cells are produced.

All-solid-state batteries (ASSBs) comprising a Li metal anode, solid-state electrolytes (SE), and cathode are ideal to meet both safety and high-energy-density requirements. By replacing a flammable solvent electrolyte with an inflammable SE, the growth of lithium dendrites can be alleviated, reducing the risk of short-circuit formation and catastrophic accidents. In this regard, various SE candidates have been proposed, such as polymers [1,2], inorganic oxide [3–5], metal halide [6], and sulfide-type compounds [7–11]. Among these candidates, a lithium argyrodite-type Li_6PS_5X (X = Cl, Br, I) has arisen as a promising candidate for SEs in ASSBs. For instance, Li_6PS_5Cl features a high Li ionic conductivity of 10^{-2} to 10^{-3} S/cm at room temperature [12], which can be explained by anion site disorder and high polarizability of sulfur [13–17]. On the flip side, a shortcoming of Li_6PS_5Cl is its phase instability related to two major decomposition pathways: electrochemical decomposition, in which the oxidation of Li_6PS_5Cl yields the side products such as LiCl, polysulfides, and elemental sulfur; and chemical decomposition at the interface between SE/active material or SE/conductive agent, triggered by adsorbed water or specific functional groups on the surface [18–22].

Recently, much attention has been paid to improving the chemical stability of SEs while maintaining the high ionic conductivity of ASSBs. In particular, within Li-argyrodite SEs containing cell, undesirable chemical reactions occur at the interface of anode/SE [18], cathode/SE [20,21], and conductive agent/SE [22]. For example, the chemical decomposition of Li_6PS_5Cl has been observed on the cathode with an oxygen-containing conductive agent [22]. Studies have reported that the addition of F-containing

* Corresponding author.
** Corresponding author.
*** Corresponding author.
E-mail addresses: sam.chen@newcastle.edu.au (X. Chen), dkkim@kaist.ac.kr (D.K. Kim), dongjun.kim@unsw.edu.au (D.J. Kim).

https://doi.org/10.1016/j.mtchem.2022.100967
2468-5194/

compounds can alleviate side reactions at the lithium metal surfaces due to the formation of LiF-enriched electrolyte interface [23]. Thus, we envisage that using graphene fluoride (GF) over conventional conductive agents could enhance the phase stability of Li_6PS_5Cl. GF is a nonstoichiometric fluorocarbon featuring semi-ionically or covalently bonded C–F in the graphene skeleton. The nature of the C–F bond can vary depending on the degree of fluorination and distribution of the fluorine [24,25]. A higher degree of fluorination changes the electron distribution of the graphene skeleton from sp^2 to sp^3 hybridization and simultaneously introduces defects, which transform the conductive character to a semi-conductive one [6,26,27].

To test our hypothesis, we introduced GF as a conductive agent and prepared a cathode composite comprising of Li_6PS_5Cl, GF, and $LiCoO_2$. Time-dependent X-ray photoelectron spectroscopy (XPS) results have revealed a significant improvement in interfacial phase stability of Li_6PS_5Cl. This might be related to fluorine dissociation that resulted in LiF formation, which presumably led to a stabilized interface between SE and a conductive agent. Furthermore, the electrochemical performances noticeably improved compared to that of containing commercial carbon black (CB) as a conductive agent. Our results demonstrate a simple and effective way to improve the vulnerable SE interface without compromising the existing battery cell structure.

2. Materials and methods

2.1. Synthesis of Li_6PS_5Cl

The Li_6PS_5Cl was prepared following the previous report [11]. Lithium sulfide (Sigma-Aldrich, 99.98% trace metals basis), phosphorus pentasulfide (Sigma-Aldrich, 99%), and lithium chloride (Sigma-Aldrich, ACS reagent, $\geq$ 99%) were mixed in the stoichiometric proportion and underwent high energy ball milling (planetary micro mill Pulverisette 7, Fritsch) for 20 h. All processes of synthesizing Li_6PS_5Cl were carried out under an argon atmosphere (O_2 < 0.5 ppm, H_2O < 0.1 ppm), and tungsten carbide jar and balls were used in the high energy ball milling.

2.2. Synthesis of GF

GF was synthesized from commercial graphite fluoride flakes (ACS material, 56–61 wt% F) using a microwave-induced exfoliation method described in a previous report [28]. Graphite flakes (Sigma-Aldrich, 332416) were used as a 'catalyst' to trigger the rapid exfoliation of graphite fluoride. The graphite flakes (~1 g) were placed in an alumina crucible (3 mL), and graphite fluoride (50 mg) was added on top without mixing. The crucible was then placed in the microwave oven (Breville, 900 W) and subjected to microwave irradiation at 900 W for 15 s in a fume hood at ambient conditions. The product was left in the fume hood for an additional 10 min to remove any gaseous species that evolved during the reaction completely. The product was then dispersed and washed in ethanol (30 mL), allowing the large graphite flakes to sink to the bottom while the exfoliated GF was temporarily stabilized in the supernatant. GF powder was separated by vacuum filtration of supernatant.

2.3. Preparation of Li_6PS_5Cl and composite electrodes

For the preparation of Li_6PS_5Cl and conductive carbon composite, the as-synthesized Li_6PS_5Cl was mixed with commercial CB (LION Chemical, ECP600JD) or prepared GF in the weight ratio of 75:5 or 96:4 by grinding with mortar and pestle. All processes were carried out under an argon atmosphere.

The composite with the weight ratio of 75:5 was stored in a sample vial and kept in an Ar-filled glove box for aging. A small amount of composite powder was retrieved after aging for 1 and 14 days to conduct time-dependent XPS analysis. The composite with the weight ratio of 96:4 was used as a working electrode for cyclic voltammetry (CV) analysis without aging time.

For the preparation of composite cathodes, conductive carbon (CB or GF), Li_6PS_5Cl, and $LiCoO_2$ (LCO, obtained from LG Chem, Republic of Korea) were mixed in a weight ratio of 1:4:5 using mortar and pestle.

2.4. Physical characterizations

X-ray powder diffraction (XRD) was carried out at room temperature using MPD (PANalytical) X'Pert multipurpose X-ray diffraction system with Cu Kα radiation (λ_1 = 1.54051 Å, λ_2 = 1.54433 Å) in Bragg–Brentano θ to θ geometry. Samples were tested using an air-tight XRD sample holder, where the powder sample was put and sealed with polyimide film under an argon atmosphere. The XRD patterns were analyzed using X'Pert HighScore Plus software.

XPS was carried out on Thermo ESCALAB250Xi high-resolution X-ray photoelectron spectrometer with a monochromatic Al Kα (1486.68 eV) X-ray source with a power of 160 W and 500 μm spot size. 100-eV pass energy was used for survey scans, 20-eV pass energy for region scans, and a photoelectron take-off angle of 90°. The resultant spectra of CB and GF were calibrated using graphite C1s peak at 284.5 eV, while Li_6PS_5Cl and composites were calibrated using adventitious C1s peak at 284.8 eV. The XPS depth profile was done by regional scans after sequential etching using Ar ion beam (1 keV). The etching schedule is 15 s for 10 times and then 30 s for 20 times. The etching rate is 0.2 nm/s on Ta_2O_5. The depth profile sample was prepared by pressing GF and Li_6PS_5Cl pellets face to face for 30 min and stored under an inert atmosphere for 7 days. The pressed pellets were separated, and the GF pellet surface was analyzed for XPS depth profile analysis.

Four-point probe method was used to measure the bulk resistivity of CB and GF pellets. The measurement was conducted on Kaivo four-point probe resistance tester with a liner four-probe. CB and GF pellets were prepared by pressing the powder under the pressure of 10 MPa, followed by measuring the thickness by a micrometer. The pellet sample was put horizontally on the stage, and the four-probe system was loaded at the center of the sample surface. The resistance (R_0) was recorded until the monitor showed a steady value. The measurement was conducted 5 times on both the top and down surfaces of a pellet sample. The measured electrical resistance and calculated electrical resistivity of GF and CB are summarized in Table S1.

Scanning electron microscopy (SEM) images were obtained using FEI Nova NanoSEM 450 field-emission scanning electron microscope. The acceleration voltage of the electron beam was 5 kV, and the spot size was 3 nm. Elemental mapping was acquired by Energy-dispersive X-ray spectroscopy (EDS) at the same SEM instrument operating at an acceleration voltage of 15 kV and spot size of 3 nm.

Transmission electron microscopy (TEM) images were obtained using JEOL JEM-F200 operating at an accelerating voltage of 200 kV. The TEM samples were prepared by directly drop-casting GF dispersion onto a 200-mesh holey carbon Cu grid.

2.5. Electrochemical characterizations

All the electrochemical evaluations were performed using 2032 coin cells at room temperature. Cyclic voltammetry was carried out

on Bio-logic (VMP3, France) potentiostat. The measurements were conducted in the voltage range of 0–4 V for 5 cycles (scan rate of 0.05 mV/s). The galvanostatic charge-discharge performance of the ASSBs was performed by Won-A-Tech battery cycler (WBCS 3000, Korea) under a constant current with cut-off voltages of 2.8 and 4.2 V vs. Li/Li^+.

3. Results and discussion

The presence and surface morphology of the prepared Li_6PS_5Cl phase were characterized using SEM and XRD. The SEM image (Fig. 1a) confirmed the granular shape with an average particle size of 1 μm. The XRD pattern (Fig. 1b) was consistent with a reference value and previous reports [11]. The broad diffraction peak in the range of $2\theta = 15–25^\circ$ was attributed to the usage of a polyimide film to prevent oxygen contact. Additionally, a small trace of tungsten carbide was identified, where the tungsten carbide phase originated from jar and ball used in planetary milling. The XPS spectra of S 2p state (Fig. S1) showed a doublet peak at 161.3 and 162.5 eV, which was assigned to the S $2p_{3/2}$ of PS_4^{3-} in the Li argyrodite. These analyses results suggest the successful synthesis of Li_6PS_5Cl.

The TEM image of the microwave exfoliated GF (Fig. 2b) displayed thin and electron-semitransparent sheets with crumples. The selected area electron diffraction pattern inset acquired from the imaging area showed diffraction spots with hexagonal symmetry, indicating a highly crystalline structure in GF sheets. A high-resolution TEM image on the edge of a GF sheet (Fig. S2) verified the few-layer structure and the formation of a highly crumpled morphology associated with the defects and residual C–F bonds, resulting in a nonplanarity of the lattice. Additionally, SEM and EDS confirmed the uniform distribution of C, O, and F elements on the GF sheets (Fig. 2c).

The XPS survey (Fig. 2d) shows the GF is composed of C (91.03 at.%), O (3.33 at.%), and F (5.34 at.%). The C/F ratio changed significantly from 1 for the starting graphite fluoride to 17 for GF. The O content in GF increased from <1 at.% for the graphite fluoride to >3 at.%, due to the oxidation of GF during rapid heating in air. The high-resolution spectra in the C 1s region (Fig. 2e) were deconvolved into five peaks corresponding to sp^2/sp^3 hybridized C–C (284.5 eV), C–O (286.0 eV), C=O (287.1 eV), C–F (290.8 eV), and CF_2 (291.9 eV). The spectra of F 1s region (Fig. 2f) showed two deconvoluted peaks, which are assigned to the covalent C–F bond and semi-ionic C–F bond [29,30]. These spectra confirm the presence of fluorine in the GF structure. To demonstrate the electrical conductivity of GF, both CB and GF were tested by the four-point probe method as the experimental section described.

The phase stability of the Li_6PS_5Cl/CB and Li_6PS_5Cl/GF composites was investigated and summarized in Fig. 3. Time-dependent XRD was conducted on Li_6PS_5Cl/CB composites on the 2nd and 14th day and compared with pristine Li_6PS_5Cl. There was no apparent difference between the XRD patterns, implying negligible changes in the existing phase. The XRD patterns of the Li_6PS_5Cl/GF composite were measured under the same conditions, which showed a similar trend with no noticeable changes in phase composition.

To gain further insights into the Li_6PS_5Cl decomposition suffered by conductive carbon, time-dependent XPS analysis (Fig. 4a) was conducted and revealed a phase change in sulfur over time. After 24 h of fabricating Li_6PS_5Cl/CB composites, new signals of elemental sulfur (S^0), oxidized compound sulfites (SO_3^{2-}), and sulfates (SO_4^{2-}) were confirmed at 162.7, 166.6, and 168.2 eV, respectively [20–22]. The sample was maintained up to 14 days of mixing, and the ratio of the sulfur derivatives consistently increased, reflecting instable nature of Li_6PS_5Cl phase. In case of P 2p state of XPS spectra (Figs. S3a and b), we did not observe phosphorus sulfides or phosphates in the chemical decomposition process. In comparison to the Li_6PS_5Cl/CB composite, the Li_6PS_5Cl/GF sample displayed substantially improved chemical stability. There was no noticeable increment after 24 h of mixing (Fig. 4b), and the side reactions were minimized up to 14 days. This observation is quite interesting as the oxygen-containing functional groups were considered as a contributor to the phase decomposition of Li_6PS_5Cl [22], but GF has a higher percentage of oxygen (3.33%) than CB (0.98%) (Figs. S4a and b).

Notably, a gradual increase in the LiF peak was confirmed at 685.5 eV within the fluorine spectra of Li_6PS_5Cl/GF (Fig. 4c). The thickness of LiF is ~15 nm, estimated by XPS depth profile analysis (Fig. S5). The LiF formation is possibly attributed to the reaction between GF and Li_6PS_5Cl, where highly ionic conductive argyrodite structure provides Li diffusion [31,32], promoting an interfacial reaction with C–F bonds. Considering the chemical stability difference between Li_6PS_5Cl/CB and Li_6PS_5Cl/GF composites, we suspect the formation of LiF-enriched layer improved the interfacial stability of the Li_6PS_5Cl/GF. Several studies have pointed out the crucial role of LiF in the formation of stable solid electrolyte interphase layer [33–35]. In addition, the C–F bond in GF can be dissociated and fluorine can act as a nucleophile [36–39]. Taken together that (i) GF has higher O content compared to CB, (ii) decomposition reaction was suppressed in the presence of GF, and (iii) the LiF peak is only observed in Li_6PS_5Cl/GF composite, we suspect that a LiF-enriched interfacial layer acts as a protective layer between Li_6PS_5Cl and GF interface.

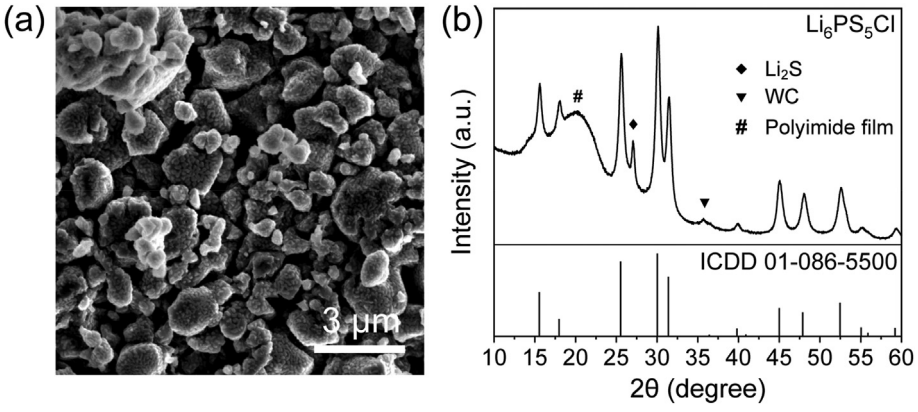

Fig. 1. (a) SEM image showing the surface morphology of Li_6PS_5Cl. (b) XRD pattern of the as-synthesized Li_6PS_5Cl (top) and the reference from the ICDD database (bottom).

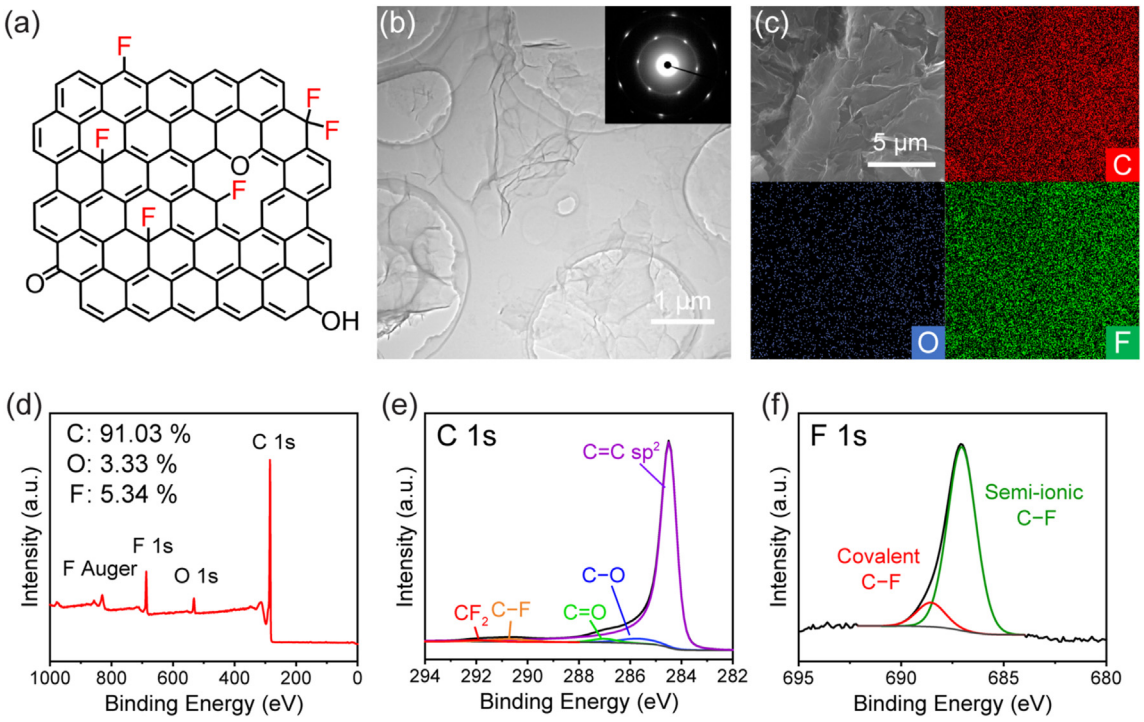

Fig. 2. (a) Chemical structure of GF (b) TEM image of GF with the selected area electron diffraction pattern (inset). (c) Elemental mapping of GF sheets measured by SEM-EDS. (d) Survey XPS spectra and high-resolution XPS spectra of (e) C 1s and (f) F 1s state of GF with Gaussian fitting results.

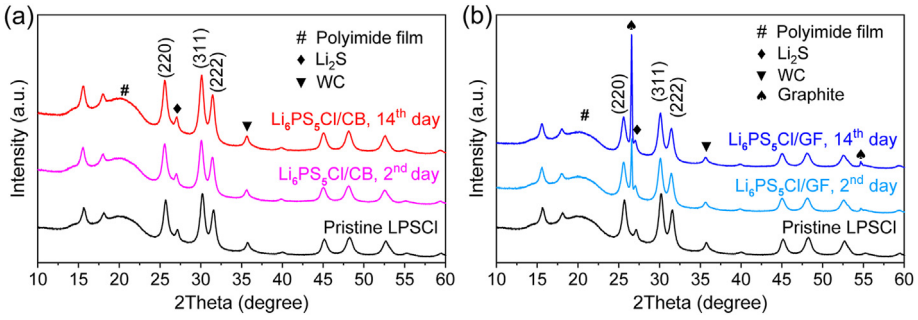

Fig. 3. XRD patterns of (a) Li_6PS_5Cl/CB and (b) Li_6PS_5Cl/GF composites after collected on the 2nd and 14th days.

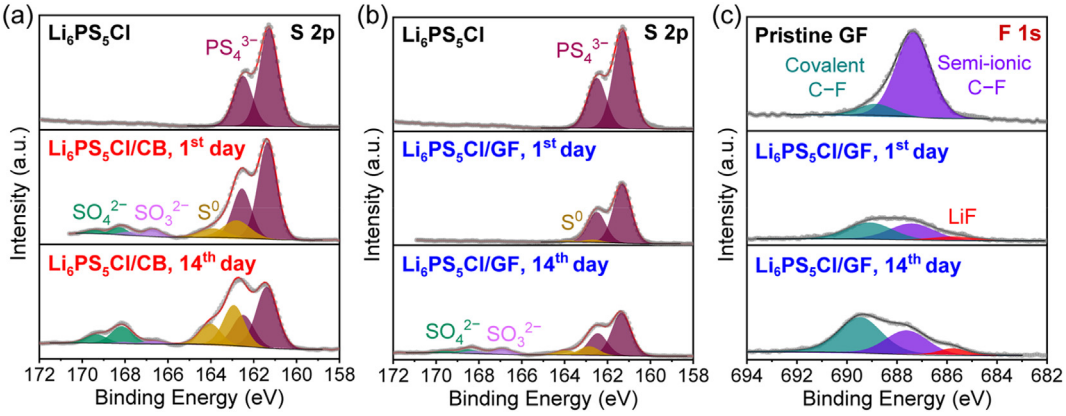

Fig. 4. XPS spectra of S 2p state of pristine Li_6PS_5Cl compared to (a) Li_6PS_5Cl/CB and (b) Li_6PS_5Cl/GF composites at 1st and 14th day. (c) XPS spectra of F 1s state of pristine GF compared to Li_6PS_5Cl/GF at 1st and 14th day.

The diminished degradation of the Li_6PS_5Cl phase in the Li_6PS_5Cl/GF composite is expected to be related to the passivation effect of LiF. Although GF inherently contains a higher content of oxygen element than the CB, our XPS results (Fig. 4) imply that the passivation driven by GF effectively stabilizes the Li_6PS_5Cl interface.

After confirming the substantially improved chemical stability of Li_6PS_5Cl by forming composite with GF, we evaluated the electrochemical performances of ASSBs. The cyclic voltammetry profile of Li_6PS_5Cl/CB displayed a significantly large anodic current at the initial cycle (Fig. 5a), which is similar to the previous report [22]. The intensity of the anodic peak was 50 mA at the 1st cycle and gradually decreased to 10–30 mA in subsequent cycles. In contrast, the Li_6PS_5Cl/GF electrode featured a reversible redox profile (Fig. 5b) that was 1000-fold lower than the CB-containing cell. It is suspected that unusual anodic current flow reflects decomposition reaction in Li_6PS_5Cl/CB.

Next, we fabricated ASSBs and performed a galvanostatic cycling test. The cathode composites were composed of a conductive agent, Li_6PS_5Cl, and $LiCoO_2$, in a weight ratio of 1: 4: 5, respectively. Hereinafter, we refer to CB comprising of the cathode as CB@SE-LCO and GF one as GF@SE-LCO. The galvanostatic profile (Fig. 5c) of both samples displayed reversible charge-discharge behavior with a single pseudo-plateau at approximately 3.8 V. In the 5th cycle, the CB@SE-LCO cell exhibited 40 mAh/g discharge capacity, while the GF@SE-LCO electrode exhibited a much higher discharge capacity of 60 mAh/g. Moreover, GF@SE-LCO featured a relatively smaller over-potential than the control CB@SE-LCO, which is possibly related to the conformal planar contact of GF. The electrochemical impedance measurement confirmed that GF@SE-LCO displayed smaller interfacial resistance than CB@SE-LCO (Fig. S7). Compared to the point contact of CB, a larger surface contact of GF is expected to alleviate current localization, which provides efficient electron pathways throughout the composite electrode [40]. The rate capability of the ASSBs at high current rates of 0.05C and 0.1C was evaluated (Fig. S8 a & b). GF@SE-LCO exhibited an enhanced capacity at 0.05C, but the performance deteriorated at 0.1C. A similar trend was observed at the CB@SE-LCO counterpart. From the cycling perspective (Fig. 5d), CB@SE-LCO showed a significant voltage drop followed by an abrupt capacity decay after the 18th

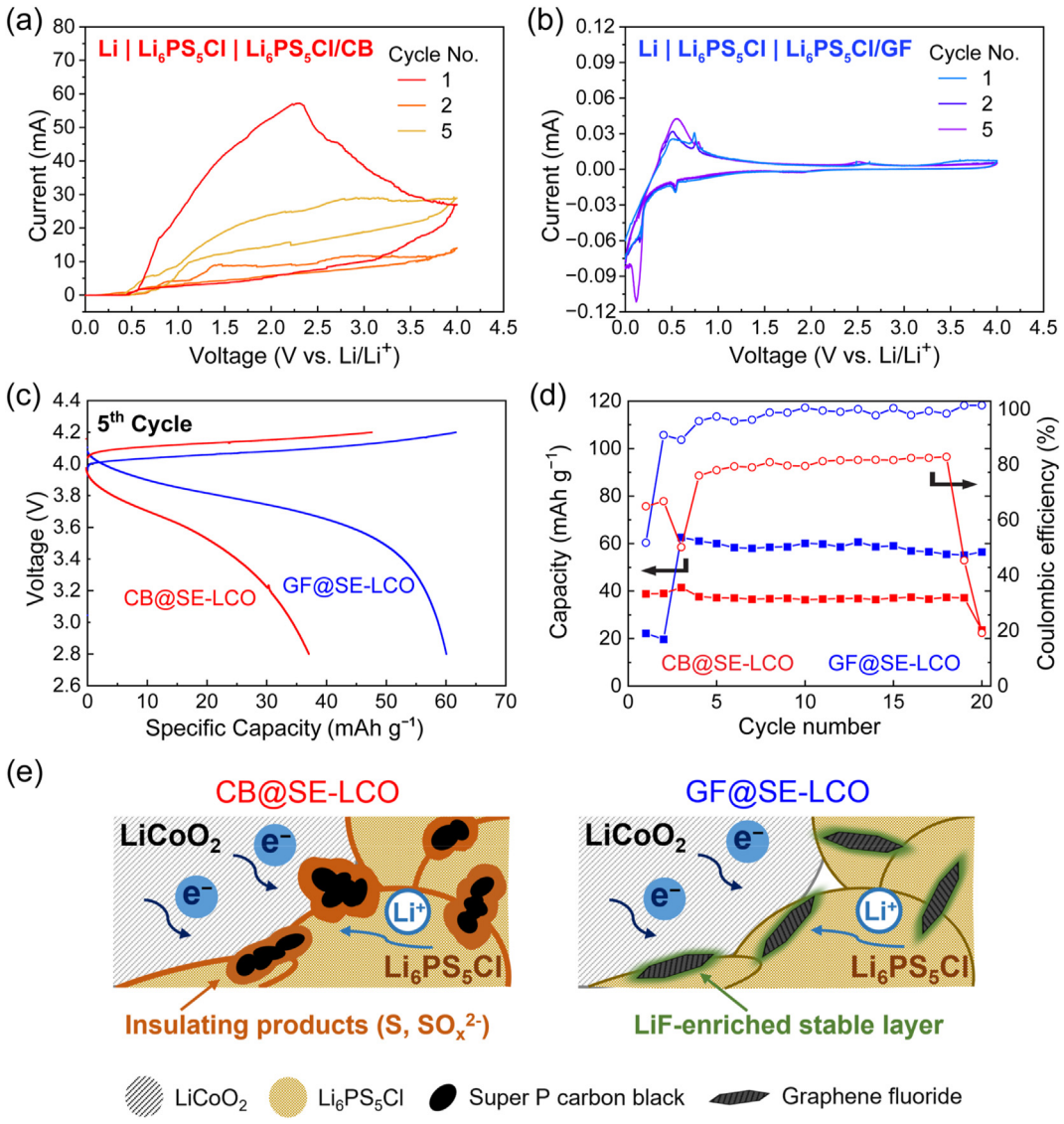

Fig. 5. CV profiles of the (a) Li_6PS_5Cl/CB and (b) Li_6PS_5Cl/GF half-cell. (c) Voltage profile of the 5th cycle and (d) cycling performance of the CB@SE-LCO and GF@SE-LCO containing cells with $LiCoO_2$ cathodes (0.034 mA, 0.025C). (e) Schematic of cathode/electrolyte interface of CB@SE-LCO and GF@SE-LCO.

cycle. In contrast, GF@SE-LCO maintained its initial capacity over 20 cycles. The average Coulombic efficiency of CB@SE-LCO and, GF@SE-LCO from the 1st~20th cycles was 72.7% and 95.5%, respectively. The relatively low Coulombic efficiency of CB@SE-LCO is attributed to the severe decomposition of SE throughout repeated cycles. On the other hand, the significantly high Coulombic efficiency of GF@SE-LCO reflects that implementing GF as conductive carbon generates LiF protective layer and effectively suppresses SE decomposition. These galvanostatic cycling results highlight the critical role of GF as a conductive material, not only as a conventional conductive agent but also to induce the formation of the LiF-enriched layer. The observation of the LiF at the Li_6PS_5Cl/GF interface (Fig. 5e) suggests that the formation of LiF can yield a stable SE/conductive carbon interface, thereby improving overall electrochemical stability.

4. Conclusion

By employing GF as a conductive agent, we attempt to address the chemical instability of Li_6PS_5Cl and the limited electrochemical performances of ASSBs. Our findings suggest a dual role of GF, providing a conductive pathway within the electrode and acting as a pivotal component of a stable interface layer. The diminishment of undesirable reactions of Li_6PS_5Cl most likely arises from the LiF-enriched layer, generated at Li_6PS_5Cl/GF interface, resulting in substantially improved electrochemical performance. Our approach shows that the formation of a conductive but chemically stable layer is a promising approach to overcome the chronic phase stability of Li-argyrodite.

Credit author statement

Xinchen Dai and **Jung Hwan Song** contributed equally to this work.

Xinchen Dai: Writing - Original draft, Methodology, Validation, Formal analysis, Investigation, Visualization. **Jung Hwan Song**: Writing - Original draft, Methodology, Validation, Formal analysis, Investigation, Visualization. **Ji Eun Wang**: Review & Editing, Methodology, Conceptualization, Validation, Formal analysis, Investigation. **Xianjue Chen**: Writing - Review & Editing, Methodology, Validation, Formal analysis, Investigation, Resources. **Do Kyung Kim**: Writing - Review & Editing, Methodology, Validation, Investigation, Resources, Supervision, Project administration, Funding acquisition. **Dong Jun Kim**: Writing – Original draft, review & editing, Conceptualization Validation, Resources. Supervision, Project administration, Funding acquisition.

Data availability

Research data are not shared.

Declaration of competing interest

The authors declare that they have no known competing financial interests or personal relationships that could have appeared to influence the work reported in this paper.

Acknowledgements

This work is dedicated to Sir Fraser Stoddart on the occasion of his 80th birthday. D.J.K. acknowledges the support from the Australian Research Council (DE210101618). D.K.K. acknowledges the support from the National Research Foundation of Korea (MSIP) (No. 2020R1A2B5B02002247), and the Technology Innovation Program (No. 20012341) funded by the Ministry of Trade, Industry & Energy (MOTIE, Korea). The authors acknowledge the Solid State & Elemental Analysis Unit (SSEAU) within the Mark Wainwright Analytical Centre (MWAC) at UNSW Sydney for the acquisition of X-ray photoelectron spectroscopy.

Appendix A. Supplementary data

Supplementary data to this article can be found online at https://doi.org/10.1016/j.mtchem.2022.100967.

References

[1] H.S. Choe, J. Giaccai, M. Alamgir, K.M. Abraham, Preparation and characterization of poly(vinyl sulfone)- and poly(vinylidene fluoride)-based electrolytes, Electrochim. Acta 40 (1995) 2289–2293.
[2] I.E. Kelly, J.R. Owen, B.C.H. Steele, Poly(ethylene oxide) electrolytes for operation at near room temperature, J. Power Sources 14 (1985) 13–21.
[3] M.A. Subramanian, R. Subramanian, A. Clearfield, Lithium ion conductors in the system $AB(IV)_2(PO_4)_3$ (B = Ti, Zr and Hf), Solid State Ionics 18–19 (1986) 562–569.
[4] Y. Inaguma, C. Liquan, M. Itoh, T. Nakamura, T. Uchida, H. Ikuta, M. Wakihara, High ionic conductivity in lithium lanthanum titanate, Solid State Commun. 86 (1993) 689–693.
[5] S. Ohta, T. Kobayashi, J. Seki, T. Asaoka, Electrochemical performance of an all-solid-state lithium ion battery with garnet-type oxide electrolyte, J. Power Sources 202 (2012) 332–335.
[6] D.K. Samarakoon, Z. Chen, C. Nicolas, X.Q. Wang, Structural and electronic properties of fluorographene, Small 7 (2011) 965–969.
[7] S. Kondo, K. Takada, Y. Yamamura, New lithium ion conductors based on Li_2S-SiS_2 system, Solid State Ionics 53–56 (1992) 1183–1186.
[8] H. Morimoto, H. Yamashita, M. Tatsumisago, T. Minami, Mechanochemical synthesis of new amorphous materials of $60Li_2S{\cdot}40SiS_2$ with high lithium ion conductivity, J. Am. Ceram. Soc. 82 (1999) 1352–1354.
[9] R. Kanno, M. Murayama, Lithium ionic conductor thio-LISICON: the Li_2S-GeS_2-P_2S_5 system, J. Electrochem. Soc. 148 (2001) A742.
[10] S.P. Ong, Y. Mo, W.D. Richards, L. Miara, H.S. Lee, G. Ceder, Phase stability, electrochemical stability and ionic conductivity of the $Li_{10\pm1}MP_2X_{12}$ (M = Ge, Si, Sn, Al or P, and X = O, S or Se) family of superionic conductors, Energy Environ. Sci. 6 (2013) 148–156.
[11] S. Boulineau, M. Courty, J.M. Tarascon, V. Viallet, Mechanochemical synthesis of Li-argyrodite Li_6PS_5X (X = Cl, Br, I) as sulfur-based solid electrolytes for all solid state batteries application, Solid State Ionics 221 (2012) 1–5.
[12] H.J. Deiseroth, S.T. Kong, H. Eckert, J. Vannahme, C. Reiner, T. Zaiß, M. Schlosser, Li_6PS_5X: a class of crystalline Li-rich solids with an unusually high Li^+ mobility, Angew. Chem. Int. Ed. 47 (2008) 755–758.
[13] L. Zhou, N. Minafra, W.G. Zeier, L.F. Nazar, Innovative approaches to Li-argyrodite solid electrolytes for all-solid-state lithium batteries, Acc. Chem. Res. 54 (2021) 2717–2728.
[14] A. Gautam, M. Sadowski, M. Ghidiu, N. Minafra, A. Senyshyn, K. Albe, W.G. Zeier, A. Gautam, M. Ghidiu, M. Sadowski, K. Albe, N. Minafra, W.G. Zeier, A. Senyshyn Heinz Maier-Leibnitz Zentrum, Engineering the site-disorder and lithium distribution in the lithium superionic argyrodite Li_6PS_5Br, Adv. Energy Mater. 11 (2021) 2003369.
[15] B.J. Morgan, Mechanistic origin of superionic lithium diffusion in anion-disordered Li_6PS_5X argyrodites, Chem. Mater. 33 (2021) 2004–2018.
[16] N. Minafra, M.A. Kraft, T. Bernges, C. Li, R. Schlem, B.J. Morgan, W.G. Zeier, Local charge inhomogeneity and lithium distribution in the superionic argyrodites Li_6PS_5X (X = Cl, Br, I), Inorg. Chem. 59 (2020) 11009–11019.
[17] C. Yu, F. Zhao, J. Luo, L. Zhang, X. Sun, Recent development of lithium argyrodite solid-state electrolytes for solid-state batteries: synthesis, structure, stability and dynamics, Nano Energy 83 (2021) 105858.
[18] S. Wenzel, S.J. Sedlmaier, C. Dietrich, W.G. Zeier, J. Janek, Interfacial reactivity and interphase growth of argyrodite solid electrolytes at lithium metal electrodes, Solid State Ionics 318 (2018) 102–112.
[19] A. Banerjee, H. Tang, X. Wang, J.H. Cheng, H. Nguyen, M. Zhang, D.H.S. Tan, T.A. Wynn, E.A. Wu, J.M. Doux, T. Wu, L. Ma, G.E. Sterbinsky, M.S. D'Souza, S.P. Ong, Y.S. Meng, Revealing nanoscale solid-solid interfacial phenomena for long-life and high-energy all-solid-state batteries, ACS Appl. Mater. Interfaces 11 (2019) 43138–43145.
[20] J. Auvergniot, A. Cassel, D. Foix, V. Viallet, V. Seznec, R. Dedryvère, Redox activity of argyrodite Li_6PS_5Cl electrolyte in all-solid-state Li-ion battery: an XPS study, Solid State Ionics 300 (2017) 78–85.
[21] J. Auvergniot, A. Cassel, J.B. Ledeuil, V. Viallet, V. Seznec, R. Dedryvère, Interface stability of argyrodite Li_6PS_5Cl toward $LiCoO_2$, $LiNi_{1/3}Co_{1/3}Mn_{1/3}O_2$, and $LiMn_2O_4$ in bulk all-solid-state batteries, Chem. Mater. 29 (2017) 3883–3890.
[22] S.W. Park, G. Oh, J.W. Park, Y.C. Ha, S.M. Lee, S.Y. Yoon, B.G. Kim, Graphitic hollow nanocarbon as a promising conducting agent for solid-state lithium batteries, Small 15 (2019) 1900235.
[23] M. He, R. Guo, G.M. Hobold, H. Gao, B.M. Gallant, The intrinsic behavior of lithium fluoride in solid electrolyte interphases on lithium, Proc. Natl. Acad. Sci. Unit. States Am. 117 (2020) 73–79.

[24] S. Zhou, S.D. Sherpa, D.W. Hess, A. Bongiorno, Chemical bonding of partially fluorinated graphene, J. Phys. Chem. C 118 (2014) 26402–26408.
[25] Y. Sato, K. Itoh, R. Hagiwara, T. Fukunaga, Y. Ito, On the so-called "semi-ionic" C-F bond character in fluorine-GIC, Carbon N. Y. 42 (2004) 3243–3249.
[26] H.Y. Liu, Z.F. Hou, C.H. Hu, Y. Yang, Z.Z. Zhu, Electronic and magnetic properties of fluorinated graphene with different coverage of fluorine, J. Phys. Chem. C 116 (2012) 18193–18201.
[27] J. Zhou, M.M. Wu, X. Zhou, Q. Sun, Tuning electronic and magnetic properties of graphene by surface modification, Appl. Phys. Lett. 95 (2009) 103108.
[28] S. Wu, J. Mo, Y. Zeng, Y. Wang, A. Rawal, J. Scott, Z. Su, W. Ren, S. Chen, K. Wang, W. Chen, Y. Zhang, C. Zhao, X. Chen, S. Wu, Y. Zeng, Y. Wang, Z. Su, W. Ren, S. Chen, C. Zhao, X. Chen, J. Mo, K. Wang, W. Chen, A. Rawal, J. Scott, Y. Zhang, Shock exfoliation of graphene fluoride in microwave, Small 16 (2020) 1903397.
[29] Y. Wang, W.C. Lee, K.K. Manga, P.K. Ang, J. Lu, Y.P. Liu, C.T. Lim, K.P. Loh, Fluorinated graphene for promoting neuro-induction of stem cells, Adv. Mater. 24 (2012) 4285–4290.
[30] W. Feng, P. Long, Y.Y. Feng, Y. Li, Two-dimensional fluorinated graphene: synthesis, structures, properties and applications, Adv. Sci. 3 (2016) 1500413.
[31] P.R. Rayavarapu, N. Sharma, V.K. Peterson, S. Adams, Variation in structure and Li^+-ion migration in argyrodite-type Li_6PS_5X (X = Cl, Br, I) solid electrolytes, J. Solid State Electrochem. 16 (2012) 1807–1813.
[32] A.R. Stamminger, B. Ziebarth, M. Mrovec, T. Hammerschmidt, R. Drautz, Ionic conductivity and its dependence on structural disorder in halogenated argyrodites Li_6PS_5X (X = Br, Cl, I), Chem. Mater. 31 (2019) 8673–8678.
[33] Z. Peng, N. Zhao, Z. Zhang, H. Wan, H. Lin, M. Liu, C. Shen, H. He, X. Guo, J.G. Zhang, D. Wang, Stabilizing Li/electrolyte interface with a transplantable protective layer based on nanoscale LiF domains, Nano Energy 39 (2017) 662–672.
[34] R. Xu, F. Han, X. Ji, X. Fan, J. Tu, C. Wang, Interface engineering of sulfide electrolytes for all-solid-state lithium batteries, Nano Energy 53 (2018) 958–966.
[35] X. Fan, X. Ji, F. Han, J. Yue, J. Chen, L. Chen, T. Deng, J. Jiang, C. Wang, Fluorinated solid electrolyte interphase enables highly reversible solid-state Li metal battery, Sci. Adv. 4 (2018), eaau9245.
[36] D.D. Chronopoulos, A. Bakandritsos, M. Pykal, R. Zbořil, M. Otyepka, Chemistry, properties, and applications of fluorographene, Appl. Mater. Today 9 (2017) 60–70.
[37] A.B. Bourlinos, K. Safarova, K. Siskova, R. Zbořil, The production of chemically converted graphenes from graphite fluoride, Carbon 50 (2012) 1425–1428.
[38] K.E. Whitener, R. Stine, J.T. Robinson, P.E. Sheehan, Graphene as electrophile: reactions of graphene fluoride, J. Phys. Chem. C 119 (2015) 10507–10512.
[39] R. Zbořil, F. Karlický, A.B. Bourlinos, T.A. Steriotis, A.K. Stubos, V. Georgakilas, K. Šafářová, D. Jančík, C. Trapalis, M. Otyepka, Graphene fluoride: a stable stoichiometric graphene derivative and its chemical conversion to graphene, Small 6 (2010) 2885–2891.
[40] K.Y. Park, J.M. Lim, N.S. Luu, J.R. Downing, S.G. Wallace, L.E. Chaney, H. Yoo, W.J. Hyun, H.U. Kim, M.C. Hersam, Concurrently approaching volumetric and specific capacity limits of lithium battery cathodes via conformal pickering emulsion graphene coatings, Adv. Energy Mater. 10 (2020) 2001216.